metals

MDPI

Article

Unlocking the Value of End-of-Life JÜLICH Solid Oxide Cell Stack Interconnect Assembly: A Combined Experimental and Thermodynamic Study on Metallic Resource Recyclability

Jeraldine Lastam [1,*], Dmitry Sergeev [1,2], Daniel Grüner [1], Michael Müller [1] and Ruth Schwaiger [1,3]

[1] Institute of Energy and Climate Research, Structure and Function of Materials (IEK-2), Forschungszentrum Jülich, 52425 Jülich, Germany; d.sergeev@fz-juelich.de (D.S.); d.gruener@fz-juelich.de (D.G.); mic.mueller@fz-juelich.de (M.M.); r.schwaiger@fz-juelich.de (R.S.)
[2] NETZSCH-Gerätebau GmbH, 95100 Selb, Germany
[3] Chair of Energy Engineering Materials, Faculty of Georesources and Materials Engineering, RWTH Aachen University, 52056 Aachen, Germany
* Correspondence: j.lastam@fz-juelich.de; Tel.: +49-24-6161-6300

Abstract: The present study provides fundamental information on the resource recyclability of the interconnect assembly, i.e., the steel interconnector and the nickel meshes, from an end-of-life JÜLICH Solid Oxide Cell Stack—F10 design. The interconnector is composed of iron, chromium, and less than 4 wt.% of other alloying elements, mainly cobalt and manganese. Calculated blended compositions with the nickel meshes revealed their potential as a raw material in the production of 4xx, 2xx, or 3xx stainless steels. The melting behavior of the interconnect assembly was investigated under different conditions, i.e., in inert and oxidizing atmospheres, with and without the addition of slag-forming fluxes. The results demonstrated preferential oxidation of chromium in a trivalent state within the stable cubic spinel phase. Finally, the experimental results were compared with the thermodynamic equilibrium calculations based on the available databases (FToxid, SGTE, and SGPS) in FactSage 8.1 software. The calculated tendency to oxidize is in the order of Cr > Mn > Fe > Co > Ni at $P(O_2)$ greater than 10^{-10} bar, validating the experimental results.

Keywords: solid oxide cell; recycling; end of life; interconnector; thermodynamic equilibrium

Citation: Lastam, J.; Sergeev, D.; Grüner, D.; Müller, M.; Schwaiger, R. Unlocking the Value of End-of-Life JÜLICH Solid Oxide Cell Stack Interconnect Assembly: A Combined Experimental and Thermodynamic Study on Metallic Resource Recyclability. *Metals* **2024**, *14*, 406. https://doi.org/10.3390/met14040406

Academic Editors: Jijun Wu and Fengshuo Xi

Received: 28 February 2024
Revised: 23 March 2024
Accepted: 25 March 2024
Published: 29 March 2024

1. Introduction

The race against time towards climate neutrality has driven several countries to adopt renewable energy alternatives, including the large-scale use of decarbonized "green" hydrogen [1,2]. The global hydrogen market is expected to grow rapidly in the coming decades to meet the climate targets set by the Paris agreement [2,3]. In Germany alone, deployment efforts are already in place to generate 90–110 TWh of energy from green hydrogen by 2030 [2,4]. In particular, the H_2Giga project was commenced in 2021 with the aim of reaching GW-scale electrolysis capacities [5]. This planned expansion will generate new waste streams in the form of end-of-life (EoL) fuel and electrolysis cells. Proactive approaches in the discussion and management of these resources must therefore be undertaken to support decarbonization efforts. In line with this, the ReNaRe subproject has been launched as a part of the H_2Giga technology platform to develop recycling and re-utilization solutions tailored to prospective electrolysis technologies [6].

Solid oxide cells (SOCs) are among the promising candidates for industrialization, owing to their superior electrical efficiency and lifetime performance [7]. Additionally, one salient feature of SOCs is their fuel feed flexibility, i.e., hydrogen, carbon monoxide, and hydrocarbons in fuel cell mode or steam and carbon dioxide in electrolysis mode, which enables the implementation of carbon capture and utilization strategies [8,9]. An illustration of a planar SOC stack developed by Forschungszentrum Jülich (JÜLICH) for

stationary applications is illustrated in Figure 1. To increase electrical capacities, individual SOCs are stacked together, with interconnectors alternately inserted between them [8]. Interconnectors have two-fold purposes: to provide a serial electrical connection between cells and to separate the oxidizing and reducing gases [8]. An SOC stack is operated at temperatures of at least 700 °C under high oxygen partial pressure gradients for long durations. Therefore, the selection of interconnector materials requires stringent criteria, i.e., they must have a compatible coefficient of thermal expansion (CTE) with the cell, strong mechanical integrity, high thermal and electrical conductivities, and cost-effectiveness. Special alloys have been developed for this purpose, such as Crofer 22 H/APU alloys by JÜLICH [10–12] and Sunfire [13] and the CFY alloy in Hexis SOC stacks [14]. In recent JÜLICH designs, special coatings are applied on the air side, while Ni meshes applied on the fuel side of the alloy improve chromium retention and electrical contact [15,16].

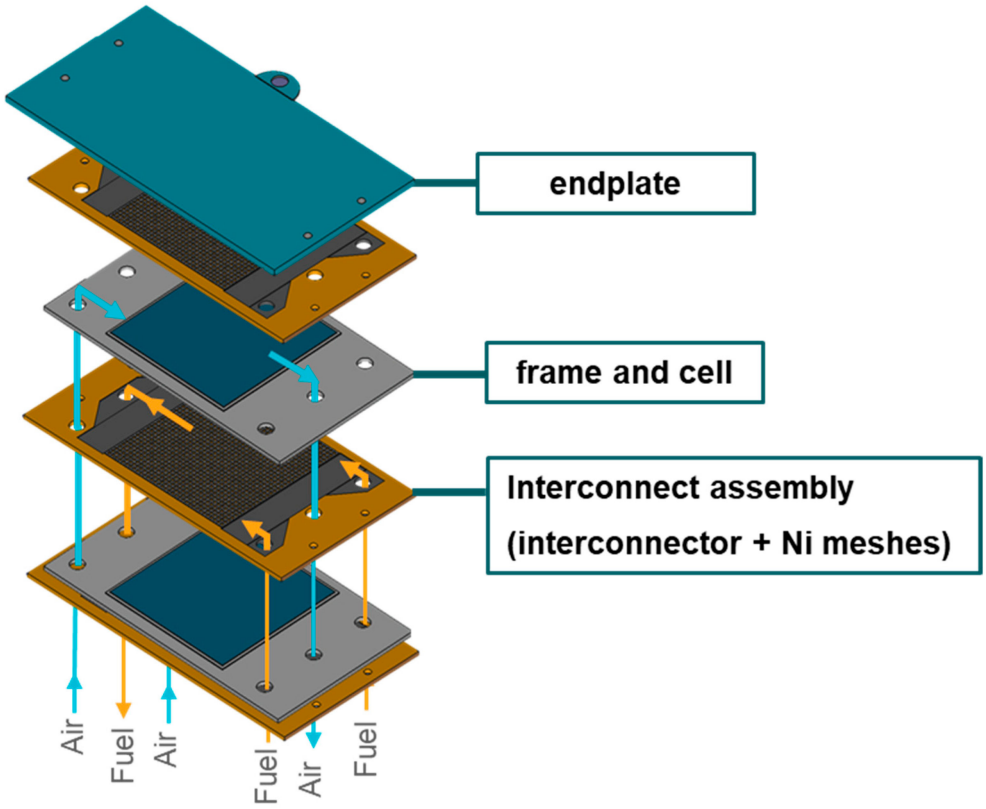

Figure 1. JÜLICH SOC F10 stack in fuel cell mode.

Manufacturers of stationary SOC stacks aim for design runtimes up to 80,000 h [16]. These values are, however, not often achieved due to cell and interconnector degradation leading to premature failure. Interconnectors suffer considerable degradation due to, among other reasons, localized gas leakages and combustion, uneven temperature distribution, and element interdiffusion in areas of direct contact with adjacent cells, all of which may result in an overall decrease in electrical conductivity and mechanical properties [11–17]. Refurbishment of EoL interconnectors might be possible, e.g., via blasting off accumulated dirt, re-coating, and heat treatment; however, up to which extent is currently not well known. Ultimately, it is not arguable that interconnectors will inevitably reach the end of their useful life and will therefore require viable recycling solutions. While studies have been made to characterize and develop recycling strategies for the ceramic cells in EoL SOC stacks [18–20], similar efforts have yet to be conducted for the interconnectors. Steel-based interconnectors from JÜLICH SOC stacks are anticipated to be of high intrinsic value, and their recovery through remelting is potentially feasible [18]. However, the level of contaminants at the end of their lifecycle remains uncertain. Therefore, this paper

provides fundamental information on the composition and metallic resource recyclability of an EoL JÜLICH SOC interconnect assembly. To achieve this, extensive sample characterization was performed, and the average compositions of the blended components, i.e., the interconnectors and the nickel meshes, were calculated. Finally, element distributions between metallic and oxide phases when melted under increasing oxidizing conditions were assessed through experimental work and thermodynamic equilibrium calculations.

2. Materials and Methods

2.1. Characterization

In the present study, an interconnect assembly consisting of an interconnector and two Ni meshes (Ni mesh 1: 2.0 × 0.6 mm^2; Ni mesh 2: 0.2 × 0.125 mm^2; mesh size × thickness) from one JÜLICH SOC stack of 10 × 10 cm^2 cells (F1004-60) was investigated. The interconnector was made up of Crofer 22 APU alloy and coated with $MnCo_{1.9}Fe_{0.1}O_4$ (MCF) and $LaMn_{0.45}Co_{0.35}Cu_{0.2}O_3$ (LCC10) coatings from the air side. The four-layer stack was operated for 3000 h at 710 °C in fuel cell mode using H_2-20%H_2O and air as fuel and oxidizing gases, respectively. The stack was then manually disassembled, and the top-most interconnect assembly was used for analysis. Specimens measuring 4 × 4 × thickness mm^3 in dimension were removed from the interconnector's longitudinal length using a laser cutting machine and subsequently divided into five zones, as shown in Figure 2. Zone 1 represents the edges of the interconnector, while zones 2 to 5 cover its inner region, as depicted in Figure 2c. Zones 4 and 5 are located on the rib-channel region in contact with the adjacent cell. Notably, Ni mesh 1 was glass-welded into the interconnector and could not be completely separated during sampling. The acronyms of techniques utilized to characterize the specimens are listed in Table 1.

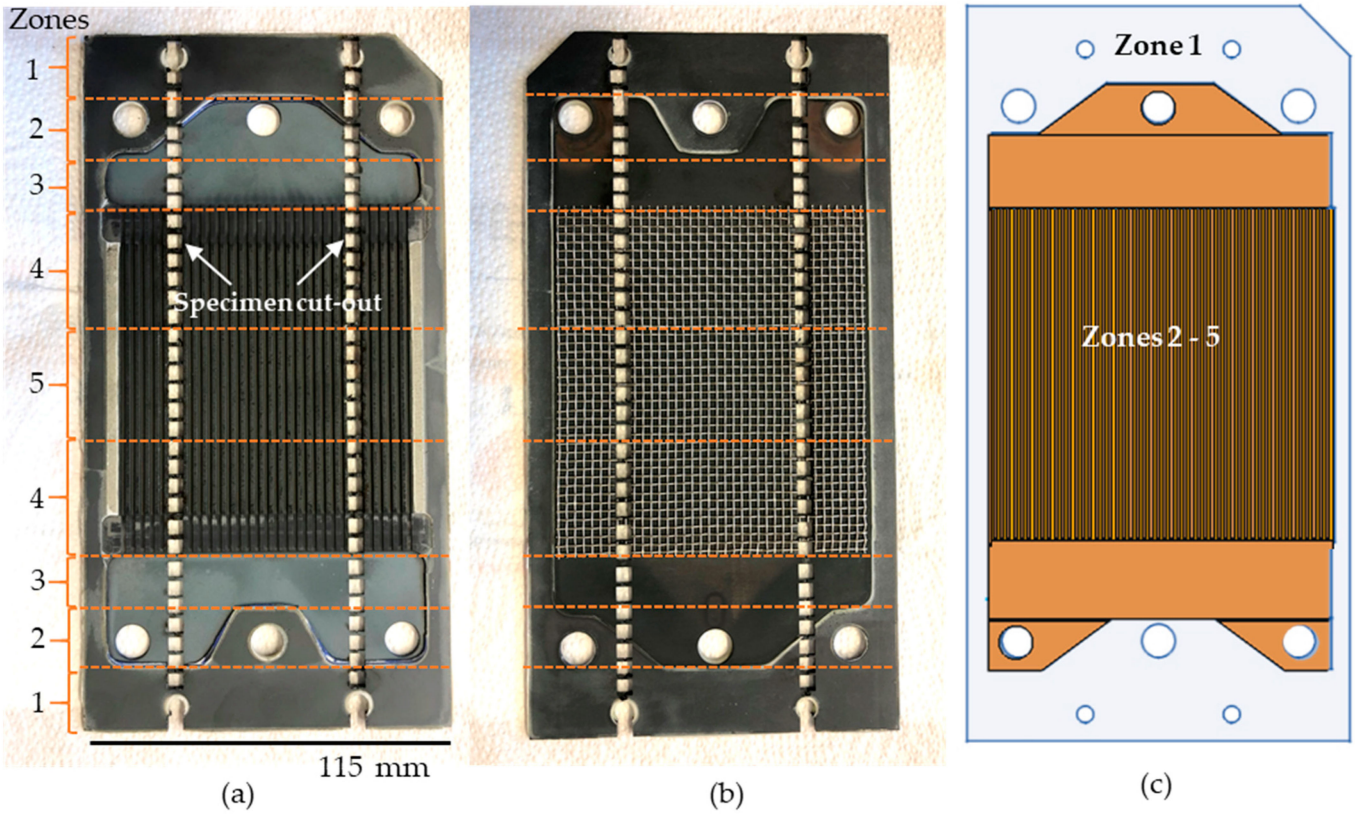

Figure 2. Photographical top view of interconnector 1 from JÜLICH SOC F10 stack on the (**a**) air side and (**b**) fuel side. Specimens are removed along its longitudinal length and divided into designated zones; (**c**) schematic illustration highlighting the compositional coverage of zone 1 in blue and zones 2 to 5 in orange.

Table 1. Nomenclature of acronyms.

Acronym	Description
SEM	Scanning electron microscope
EDS	Energy-dispersive X-ray spectroscopy
ICP-OES	Inductively coupled plasma–optical emission spectroscopy
DTA	Differential thermal analysis
DSC	Differential scanning calorimetry
CAD	Computer-aided design
XRD	X-ray diffraction
BSE	Backscattered electrons
TGA	Thermogravimetric analysis
EBSD	Electron backscatter diffraction

Three sets of zonal specimens, each specimen weighing between 250 and 350 mg, were collected for characterization. The first set was coated with gold approximately 10 nm thick via sputtering to minimize electric charging during imaging. This was followed by nickel electroplating to deposit a nickel layer about 10 µm thick to preserve the oxides. Subsequently, the specimens were embedded in epoxy resins, ground, and polished. The polished surfaces were then analyzed with an SEM (MERLIN, Zeiss, Oberkochen, Germany) equipped with EDS (X-max 80, Oxford Instruments, High Wycombe, UK). Pure elements were used as standards for quantitative EDS analysis. The specimens from the second set were analyzed with an ICP-OES (iCAP 7600, Thermo Fisher Scientific, Waltham, MA, USA). On the last set, DTA (STA 449 C, NETZSCH equipped with rhodium furnace and Al_2O_3 protective tube) was performed to determine phase transition temperatures. A schematic of the device used for DTA is shown in Figure 3a. DTA signals were recorded using a DSC sample holder (Type S, Pt/Pt10%Rh thermocouple), as illustrated in Figure 3b. Zonal specimens were then placed in Pt/Rh crucibles with Al_2O_3 liner, heated to 1600 °C at 15 °C/min and then held for 5 min under 40 mL/min argon gas. A METROTEC oxygen sensor detected an O_2 content of around 620 ppm in the outflow gas stream. Transition temperatures were recorded from the second or third cycle when sample homogeneity was ensured. Temperature calibration was also conducted to ensure accurate phase transition temperatures. This involved heating up standard pure substances (In, Sn, Bi, Zn, Al, Ag, Au, and Ni) above their melting temperatures and adjusting the measured endothermic onset peaks to align with their known melting points. A calibration curve, derived from the differences between measured and reference melting points, was obtained and subsequently used to correct the experimental transition temperatures. To calculate the blended compositions, a three-dimensional CAD model was created using the open-source FreeCAD 0.19 software. The volumes of the various parts of the model were determined through geometric calculations by this software, and corresponding masses were calculated using reference densities. Finally, the blended compositions were determined from the component masses and the elemental composition of the specimens obtained from ICP-OES analyses.

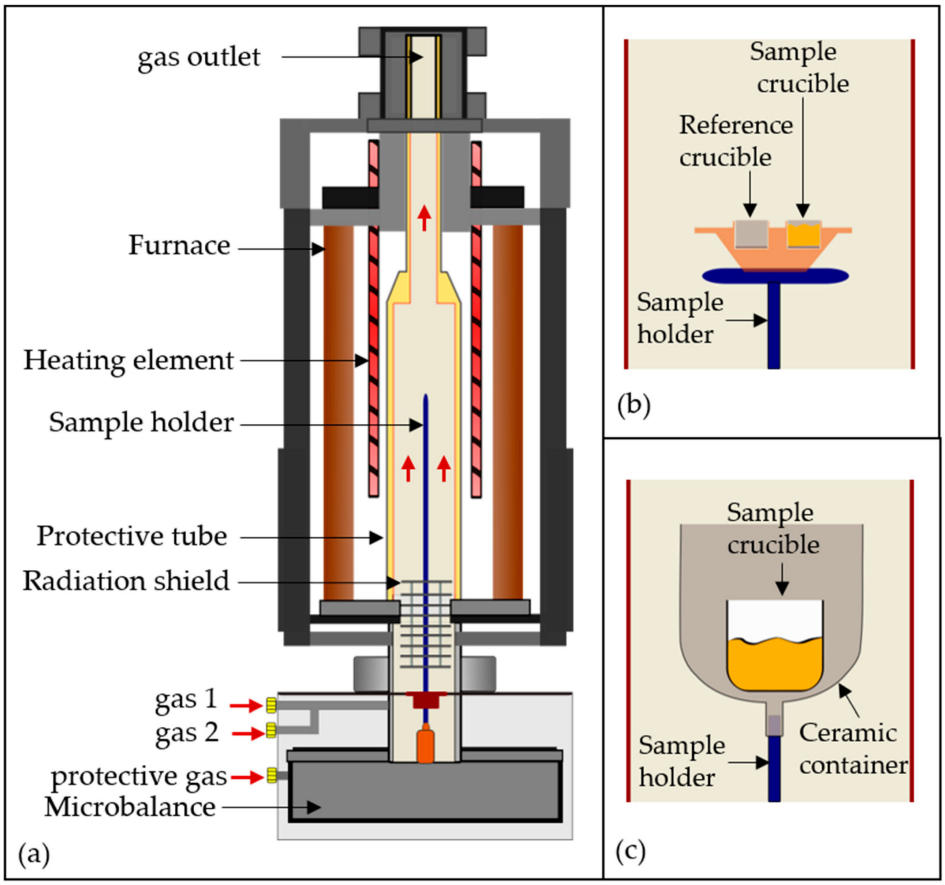

Figure 3. (**a**) Schematic of the used NETZSCH STA device; sample holder layout for (**b**) DTA and (**c**) remelting and smelting experiments.

2.2. Remelting and Smelting Experiments

To evaluate the element distribution between the metallic and oxide phases under increasing oxygen partial pressures, representative samples of approximately 1700 mg each were utilized in this study. The samples were comprised of zonal specimens and nickel mesh and possessed compositions close to that of the interconnect assembly. The samples underwent a series of remelting (without fluxes) and smelting (with fluxes) experiments. In the smelting experiments, lime and silica fluxes were added at a ratio of CaO/SiO_2 = 1.7 (*w/w*) and 10 wt.% of the sample. This ratio was decided based on the recommended basicity range of chromium-bearing steel slags to achieve optimum chromium recovery [21–23]. Readily available amorphous SiO_2 powder (Alfa Aesar, Kandel, Germany, 99.5%) was used, whereas CaO was obtained by decomposing $CaCO_3$ (VWR, Leuven, Belgium, 99.0%) at 1000 °C for 3 h. An XRD analysis with PANalytical EMPYREAN Diffractometer (Malvern, UK) using Cu Kα radiation in a Bragg–Brentano geometry confirmed the powder purity at around 95 wt.% CaO and 5 wt.% $Ca(OH)_2$. The fluxes were then combined and sintered at 800 °C for 3 h. Experiments were performed using the NETZSCH STA 449 F3 Jupiter ® equipped with graphite furnace and Al_2O_3 protective tube. Samples weighing between 1600 and 1800 mg were placed within open 0.7 mL Al_2O_3 crucibles (KYOCERA, Mannheim, Germany). These crucibles were then positioned inside open 3.4 mL Al_2O_3 crucibles (NETZSCH, Selb, Germany) and fixed to the sample holder that also serves as a type-S thermocouple. The sample holder layout is shown in Figure 3c. The furnace was purged with argon gas and evacuated twice to remove any atmospheric oxygen. The furnace was then heated to 1600 °C and held for 30 min under increasing oxygen partial pressures at heating and cooling rates of 10 °C/min. Thermogravimetric analyses (TGAs) were simultaneously performed wherein sample weight changes were recorded during

heating and cooling cycles. Experimental conditions used are listed in Table 2. Ultrapure argon and oxygen gases (99.9992 vol. %) provided by AIR PRODUCTS (Germany) were utilized. The total gas flow rates and pressures were constant at 60 mL/min and 1 bar, respectively. Subsequently, samples were cross-sectionally cut, embedded in resins, ground and polished, and analyzed with SEM and EDS. The results were compared with equilibrium thermodynamic calculations based on the available databases (FToxid, SGTE, SGPS) in FactSage 8.1 software. All oxide phases in FToxide and all metallic phases in SGTE and SGPS thermodynamic databases were employed in the calculations.

Table 2. Experimental conditions.

Experiment	Sample Code	Ar/O_2 Gas Mixture (mL/min)	Calculated $P(O_2)$ (Bar)
Remelting	R0	60/0	0
	R1	55/5	0.08
	R2	50/10	0.17
	R3	40/20	0.33
Smelting	S0	60/0	0
	S1	55/5	0.08
	S2	50/10	0.17
	S3	40/20	0.33

3. Results and Discussion

3.1. Sample Characterization

Figure 4a shows the cross-sectional microstructural layers on the zone 4 specimen. On the air side of the Crofer 22 APU alloy substrate, there were two main oxide layers—a perovskite top layer based on LCC10 and a second spinel layer based on the MCF coating. The perovskite and spinel layers were measured to be 96 and 132 µm thick, respectively, while the bulk of the thickness was attributed to the alloy substrate. The outermost Ni layers were incorporated via electroplating during the metallographic sample preparation to preserve the structural integrity of the oxide coatings. Additionally, thermally grown Cr_2O_3 and Cr_2MnO_4 were present along the alloy interfaces in both fuel and air sides. The oxide coating stoichiometric formulas were calculated based on the average atomic composition from three EDS point analyses per oxide (Figure 4b). The results revealed minor differences from the reference formulas of the coatings. BSE images and phase images derived from EDS mapping of the alloy–MCF coating interface (Figure 4c) showed the presence of an oxide layer, $Mn_{0.6}Co_{1.35}Cr_{1.05}O_4$, approximately 6 µm thick. This layer served as an interdiffusion zone between the MCF and Crofer 22 APU regions.

The perovskite and spinel coatings were similarly present in zones 2 to 5 (not shown), although they were absent in zone 1. Instead, a glass matrix consisting of Al, Si, and Ca oxides was found (Figure 4d) in a few zone 1 specimens. This can be attributed to the Type 87 ZYBF-2 glass sealant used to join the stack components. Finally, Ni mesh 1 was present on some welded areas in zones 4 and 5 due to the difficulty in completely detaching the mesh (Figure 4e).

The elemental compositions shown in Table 3 and based on ICP-OES analyses indicate that the zonal specimens were predominantly composed of Fe and Cr, while other alloying elements made up less than 4 wt.%.

Among the minor alloying elements, Co and Mn were the most abundant, with an average of 1.74 and 1.42 wt.%, respectively. This was expected due to the relatively thicker MCF layer compared to other oxide layers. The concentration of Co and Mn was lowest in zone 1, indicating the absence of MCF coating in this region. The concentration of La was highest in zones 4 and 5 at 0.81 and 0.58 wt.%, respectively, demonstrating the exclusive presence of perovskite coating on the active region in direct contact with the cell. The concentration of Ni was minimal at <0.1 wt.% for all zonal specimens; therefore, mesh sintering on non-welded areas was insignificant. The presence of Ca, Al, and Si

from the glass sealant in zone 1 was not demonstrated here due to its absence on the analyzed specimen.

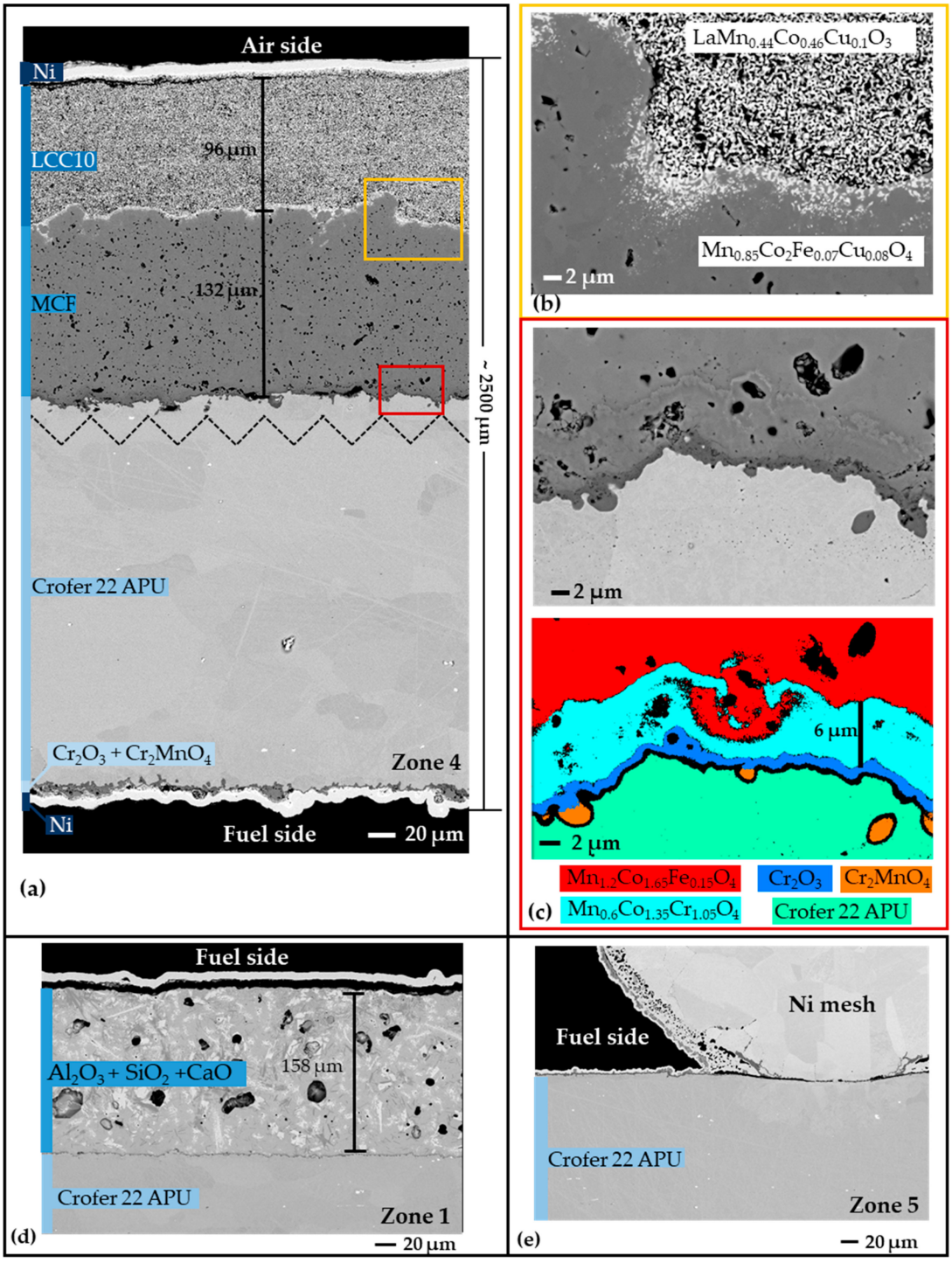

Figure 4. (**a**) Cross-sectional BSE images of zone 4 specimen. Spliced region is denoted by broken lines; (**b**) BSE image of the LCC10-MCF interface. The actual stoichiometric formulas showed little variation compared to the reference formulas (LCC10: $LaMn_{0.45}Co_{0.35}Cu_{0.2}O_3$; MCF: $MnCo_{1.9}Fe_{0.1}O_4$); (**c**) BSE and phase images (derived from EDS data) of the MCF–alloy interface; (**d**) a glass composite on the fuel side of a specimen from zone 1; (**e**) welded Ni mesh on the fuel side in a specimen from zone 5.

Table 3. Elemental composition and standard deviation (wt.%) values of zonal specimens.

Element	Zone 1	Zone 2	Zone 3	Zone 4	Zone 5	Mean (Zones 2–5)
Fe	76.3 ± 0.03	74.3 ± 0.60	73.76 ± 0.60	74.4 ± 0.60	73.7 ± 0.90	74.2 ± 0.63
Cr	22.9 ± 0.11	22.2 ± 0.10	22.0 ± 0.30	22.3 ± 0.30	22.2 ± 0.30	22.2 ± 0.24
Co	0.00 ± 0.002	1.83 ± 0.030	2.32 ± 0.040	1.21 ± 0.040	1.60 ± 0.040	1.74 ± 0.034
Mn	0.52 ± 0.005	1.45 ± 0.050	1.77 ± 0.050	1.15 ± 0.050	1.31 ± 0.050	1.42 ± 0.045
La	0.09 ± 0.003	0.09 ± 0.003	0.09 ± 0.003	0.81 ± 0.007	0.58 ± 0.019	0.39 ± 0.009
Ni	0.02 ± 0.001	0.02 ± 0.001	0.02 ± 0.001	0.06 ± 0.002	0.09 ± 0.001	0.05 ± 0.001
Traces	0.13 ± 0.005	0.08 ± 0.008	0.05 ± 0.003	0.05 ± 0.003	0.05 ± 0.002	0.06 ± 0.005

DTA measurements of the zonal specimens in Figure 5 show that the onset temperatures of the endothermic peaks, which correspond to melting points, range from 1514 °C to 1519 °C. These temperatures fell within the expected range for Crofer 22 APU (1510–1530 °C) [24], suggesting a negligible influence of the coatings on the alloy substrate's melting point. Additionally, small endothermic peaks between 500 °C and 700 °C suggested the occurrence of solid–solid transformations. The experimental melting temperatures of zonal specimens were within ±3 °C from the melting temperature in the Fe-Cr binary phase diagram calculated with FactSage 8.1 using the SGTE database (Figure 6).

The melting point of Ni mesh 2 was found to be 2 °C lower than that of the pure Ni (1454 °C) obtained through temperature calibration as described in Section 2.1, indicating the high purity of the mesh. Therefore, it can be concluded that the Ni mesh is unaffected by operation and can be treated as pure for the sake of analysis. Conversely, exothermic peaks revealed severe undercooling (16–36 °C). Hence, the recorded crystallization temperatures were not reliable.

The interconnector volume was determined from the CAD model created using FreeCAD 0.19 software. Due to significant compositional variation between zone 1 and the region covering zones 2 to 5, their volumes were calculated separately. Corresponding mass values were determined based on these volumes and the reference densities for Crofer 22 APU [24]. The volume and mass of Ni mesh 1 were calculated similarly using the reference density for Ni [25]. In contrast, the mass of the detached Ni mesh 2 was directly measured. Table 4 presents the volume and mass values of the components. Using the composition of the interconnector regions, and assuming that the meshes were of pure Ni, blended compositions were computed and are shown in Figure 7. Accordingly, there are three steel families close to these compositions—AISI 4xx, 2xx, and 3xx series steels. Selected lean steel grades with the closest compositions are listed in Table 5. Production of a 4xx-series steel product through the manufacture of Crofer 22 APU enables closed-loop recycling; however, this path highly depends on the successful separation of the interconnector from welded Ni meshes upon stack dissection. One viable approach to this is via automated stack dismantling with the use of artificial intelligence [18]. On the other hand, open-loop recycling is possible via the production of 2304 and 304 steels.

Table 4. Component volumes and masses.

Component	Volume (mm^3)	Mass (g)
Interconnector * (Zone 1)	21,564.60	166.0
Interconnector (Zones 2–5)	29,694.51	228.6
Ni mesh 1 **	2424.10	21.6
Ni mesh 2	-	13.6

Density: * Crofer = 7.7 g/cm^3; ** Ni = 8.9 g/cm^3.

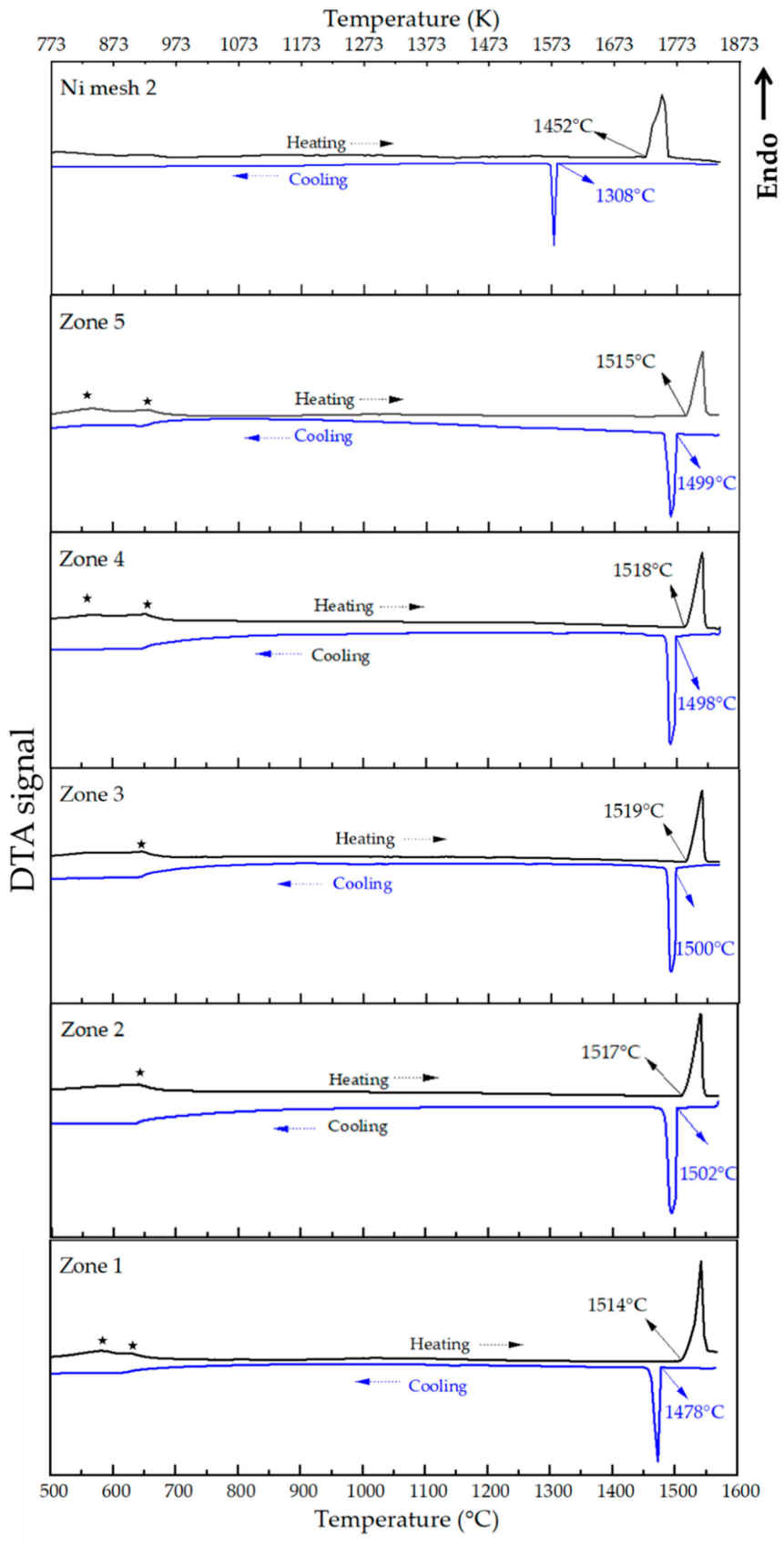

Figure 5. DTA signals of zonal samples and Ni mesh 2. Onset values of major endothermic peaks correspond to melting points while smaller peaks highlighted by star symbols (*) may indicate solid state transitions.

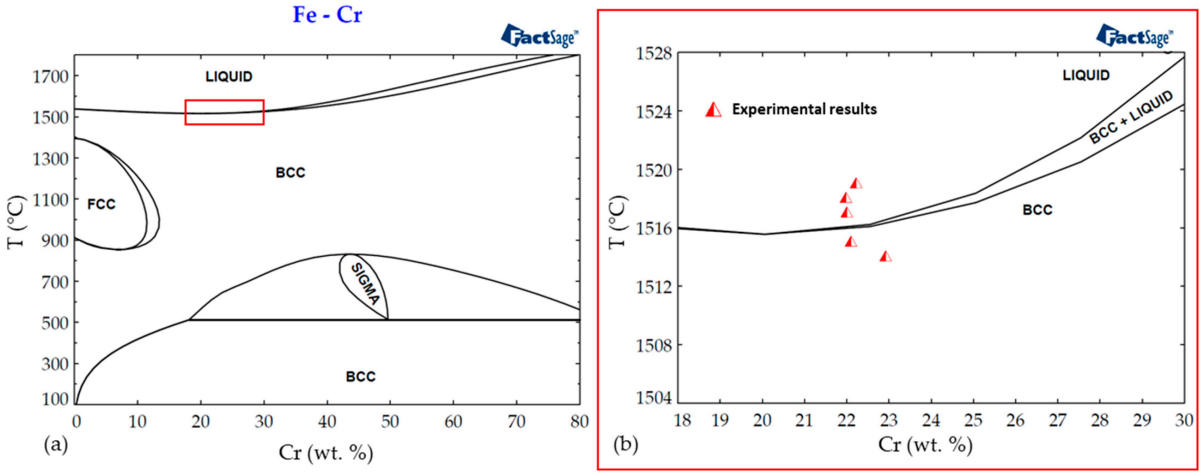

Figure 6. (**a**) Fe-Cr equilibrium phase diagram calculated with FactSage 8.1; (**b**) zoomed-in region with plotted experimental melting points of zonal specimens.

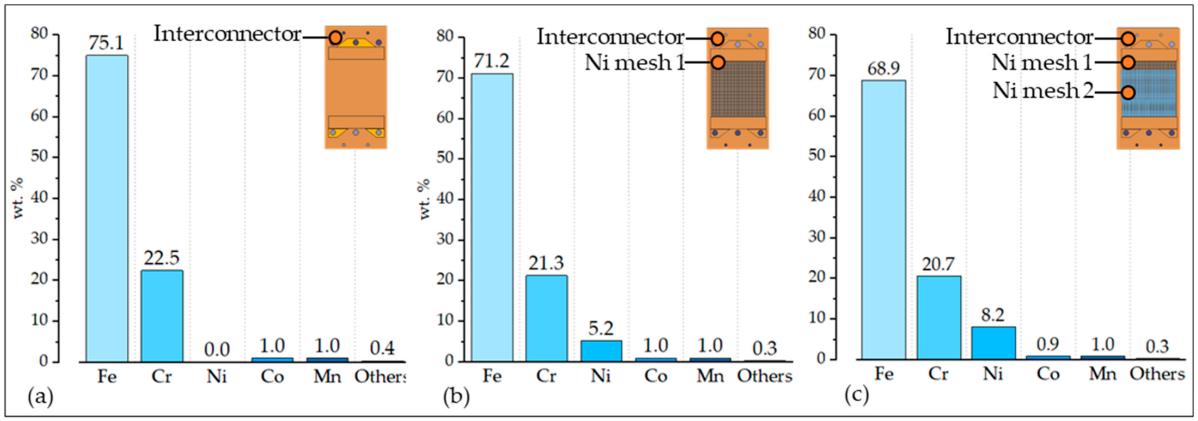

Figure 7. Composition of the interconnect assembly (**a**) without Ni meshes, (**b**) with Ni mesh 1, and (**c**) with Ni meshes 1 and 2.

Table 5. Elemental composition (wt.%) of selected steel products from AISI 4xx, 2xx, and 3xx series.

AISI Series	Grade	EN No.	Fe	C	Cr	Ni	Mn	Si	Others	Others	Ref.
4xx	Crofer 22 APU	1.4760	Bal	≤0.030	20.0/24.0	-	0.50	≤0.50	≤0.050 P	≤0.020 S	[24]
2xx	2304	1.4362	Bal	≤0.030	22.0/24.0	3.5/5.5	≤2.00	≤1.00	≤0.035 P	≤0.015 S	[26]
3xx	304	1.4301	Bal	≤0.07	17.5/19.5	8.0/10.0	≤2.00	≤1.00	≤0.045 P	≤0.015 S	[26]

3.2. Thermogravimetric Analysis

In Table 6, the mean predicted compositions and standard deviations of the representative samples are given. Remelted and smelted samples pertain to samples with and without the addition of 1.7CaO/SiO_2 (*w/w*) fluxes at 10 wt.% to the total feed. Both the remelted and smelted samples were observed to exhibit a relatively equal mass increase when exposed to low P(O_2) up to 0.17 bar (Figure 8). However, a substantial deviation occurred beyond this level, from which remelted samples experienced twice the weight increase compared to smelted samples. This demonstrates the beneficial effect of oxide fluxes in inhibiting oxidation, which was particularly evident under high oxidizing conditions. Notably, one remelted sample exposed to P(O_2) = 0.33 bar underwent complete oxidation while the corresponding smelted sample was only moderately affected.

Table 6. Mean and standard deviation (wt.%) values of predicted elemental composition of representative samples.

Element	Composition (wt.%)
Fe	68.4 ± 0.43
Cr	20.2 ± 0.61
Ni	8.5 ± 0.25
Co	1.3 ± 0.01
Mn	1.0 ± 0.35
La	0.3 ± 0.15
Traces	0.1 ± 0.02

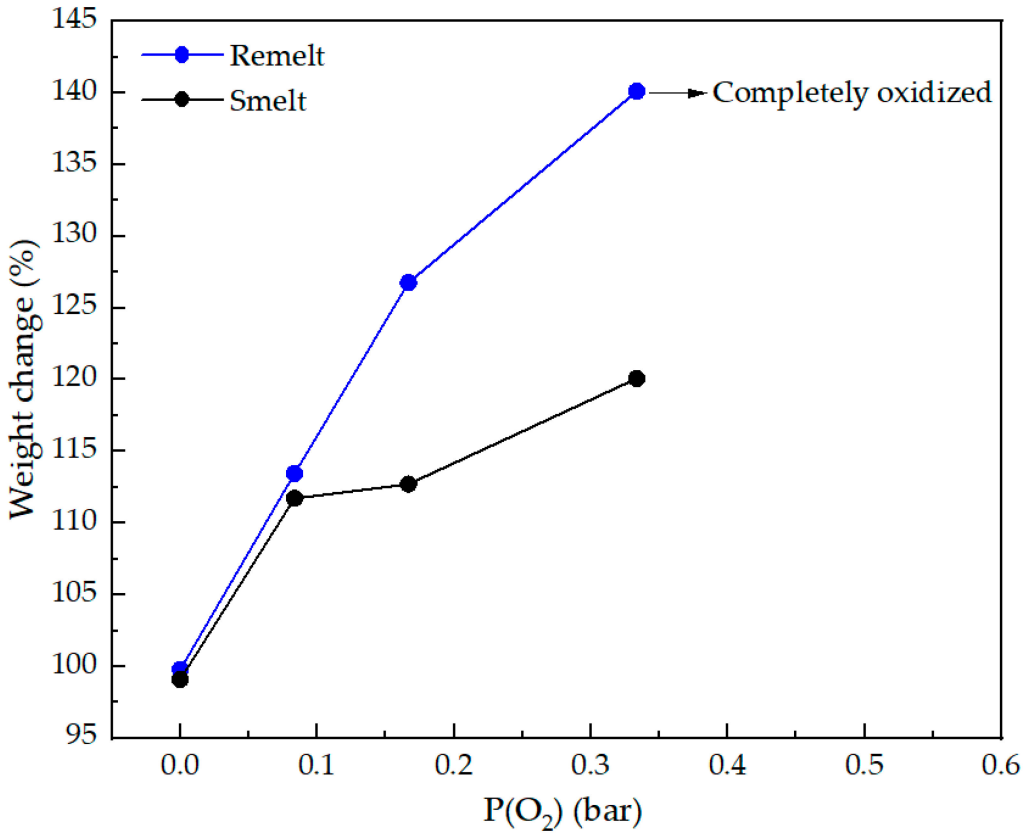

Figure 8. Weight change (%) in remelted and smelted samples as a function of $P(O_2)$. Initial weights correspond to sample weight for remelting and sample and flux total weights for smelting experiments, respectively.

The results from TGA as shown in Figure 9 demonstrate an overall weight increase as a function of $P(O_2)$, assumed to be correlated to the quantity of oxygen absorbed by the sample to form oxide phases. Notably, oxidation reactions started at earlier timepoints in smelted samples compared to remelted samples. This was likely due to slag forming at lower temperatures in smelted samples, as supported by the oxide phase distributions (wt.%) calculated with FactSage 8.1 (SGTE, SGPS, and FTOxid databases) and shown in Figure 10. According to calculations, slag starts to form at a lower temperature (1243 °C) in a smelted sample in contrast to a remelted sample when both are subjected to atmospheric air condition. On the other hand, the completion of oxidation could be temperature-dependent, as evident from the observed slowing down of weight changes upon cooling.

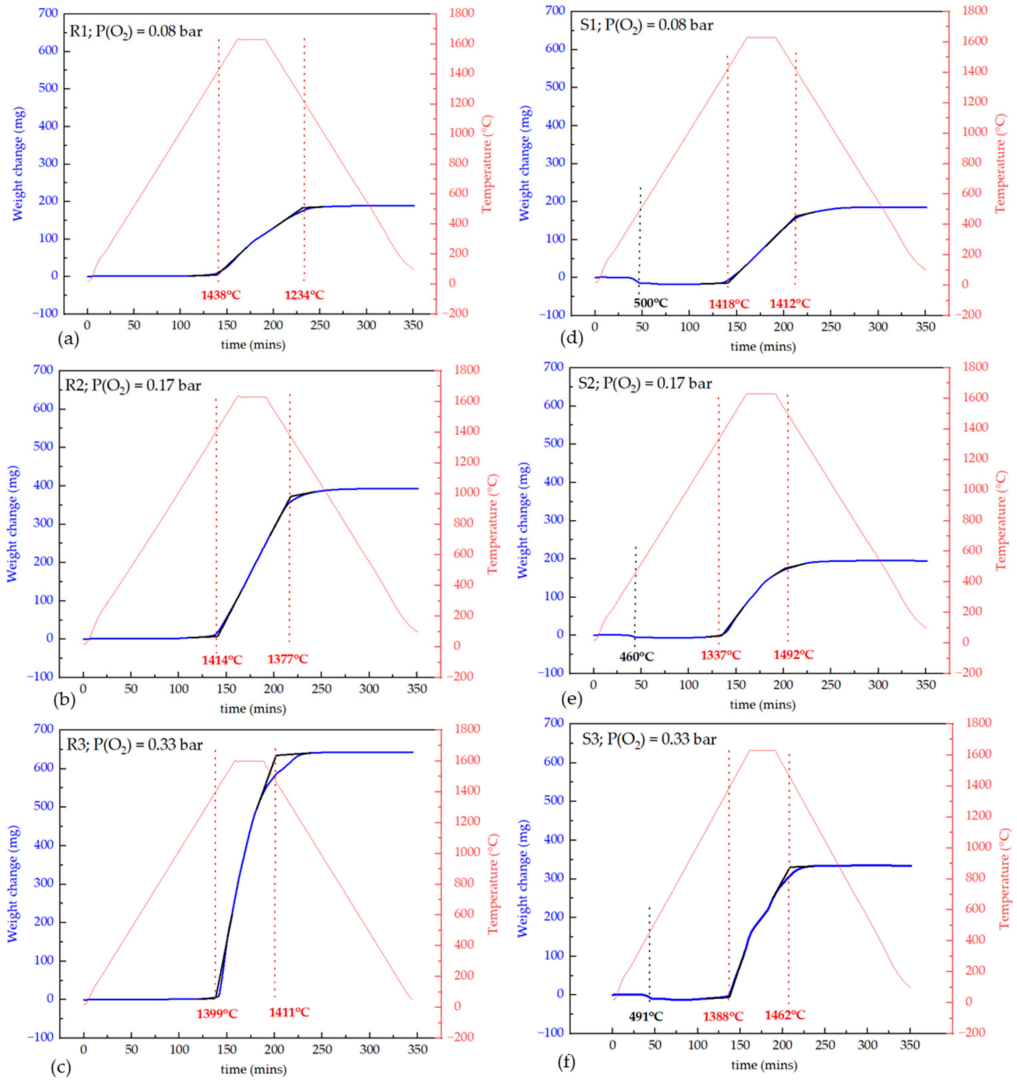

Figure 9. TGA profiles for remelted and smelted samples at 1600 °C as a function of $P(O_2)$: (**a**,**d**) $P(O_2)$ = 0.08 bar, (**b**,**e**) $P(O_2)$ = 0.17 bar, and (**c**,**f**) $P(O_2)$ = 0.33 bar, respectively. Weight changes (%) are indicated by blue solid lines, while temperature–time profiles are depicted by red solid lines. Vertical red dotted lines mark the approximate start and end temperatures for oxidation reactions. Sample weights exhibited a dramatic increase with increasing $P(O_2)$ from specific start temperatures and slowed down upon cooling from the maximum temperature. Notably, smelted samples showed an earlier weight increase compared to remelted samples. Finally, vertical black dotted lines indicate the temperatures at which residual $Ca(OH)_2$ presumably decomposed.

Finally, a dip in weight change between 460 °C and 500 °C was observed only in smelted samples in Figure 9. This could be explained by the thermal dehydration of residual $Ca(OH)_2$ from the CaO-SiO_2 flux mixture. The corresponding reaction enthalpy and equilibrium temperature as calculated from FactSage 8.1 using the FactPS database are shown:

$$Ca(OH)_2(s) \rightarrow CaO(s) + H_2O(g);\ \Delta H = +\ 99.46\ kJ/mol,\ T = 524\ °C$$

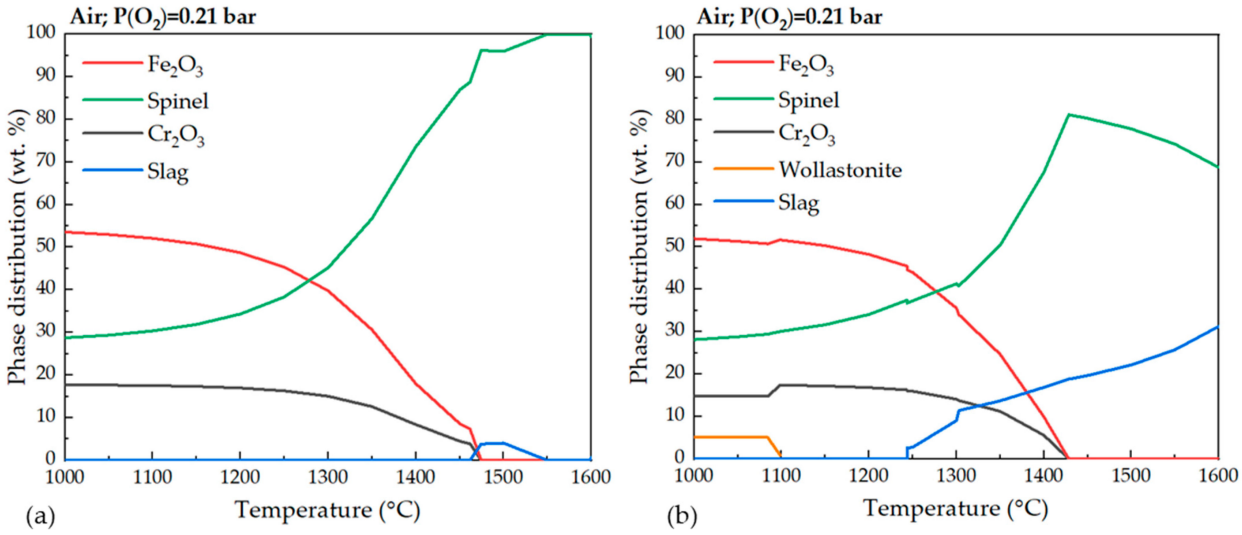

Figure 10. Calculated equilibrium oxide phase distribution as a function of temperature under atmospheric air for (**a**) remelted and (**b**) smelted samples. Curves in the plots correspond to specific phases with the following color scheme: red for Fe_2O_3, green for spinel, black for Cr_2O_3, blue for slag and orange for wollastonite. Minor phases less than 2 wt.% fractions are excluded.

3.3. Microstructural Analysis of Oxide and Metallic Phases

The oxide phases near the alloy–oxide interface were analyzed, where equilibrium phases that formed at 1600 °C were likely quenched and preserved. The metallic phases in the center of the alloy specimens were also investigated. The phase atomic compositions and stoichiometric formulas were determined by averaging 3 to 5 EDS point analyses per phase. Table 7 lists the oxide phases and their compositions, and Figure 11 depicts the corresponding BSE images on the alloy–oxide interface.

Table 7. Oxide phases observed on the alloy–oxide interfaces in remelted and smelted samples. Chemical compositions of slags exclude minor phases constituting less than 2 wt.%.

Sample Code	Phase	Stoichiometric Formula/ Chemical Composition	Short Notation
R0	Spinel Lanthanum chromium oxide	$Cr_{2.4}(Mn, Al)_{0.8}O_4$ $CrLaO_3$	Spin CrLa
R1	Spinel Chromia	$(Cr)_2(Fe, Mn, Ni)O_4$ Cr_2O_3	Spin Chro
R2	Spinel Wüstite	Cr_2FeO_4 FeO	Spin Wus
R3	Spinel Hematite	$(Cr, Fe)_2(Ni, Co, Fe)O_4$ $Fe_{1.5}(Cr, Ba, La)_{0.5}O_3$	Spin Hem
S0	Hibonite Calcium aluminosilicate Anorthite	$(Ca)(Al_{0.9}Cr_{0.1})_{12}O_{19}$ $Ca_2Al_2SiO_7$ $CaAl_2Si_2O_8$	Hib CAS Ano
S1	Spinel Chromia Slag	$(Cr_{0.9}Al_{0.1})_2(Fe_{0.7}Ni_{0.10}Mn_{0.20})O_4$ $Cr_{1.8}Al_{0.2}O_3$ $26CaO\text{-}46SiO_2\text{-}25Al_2O_3\text{-}3FeO$ (wt.%)	Spin Chro Slag
S2	Spinel Slag	$(Cr_{0.9}Al_{0.1})_2(Fe_{0.8}Mn_{0.20})O_4$ $13CaO\text{-}66SiO_2\text{-}12Al_2O_3\text{-}9FeO$ (wt.%)	Spin Slag
S3	Spinel Slag	Cr_2FeO_4 $11CaO\text{-}61SiO_2\text{-}11Al_2O_3\text{-}17FeO$ (wt.%)	Spin Slag

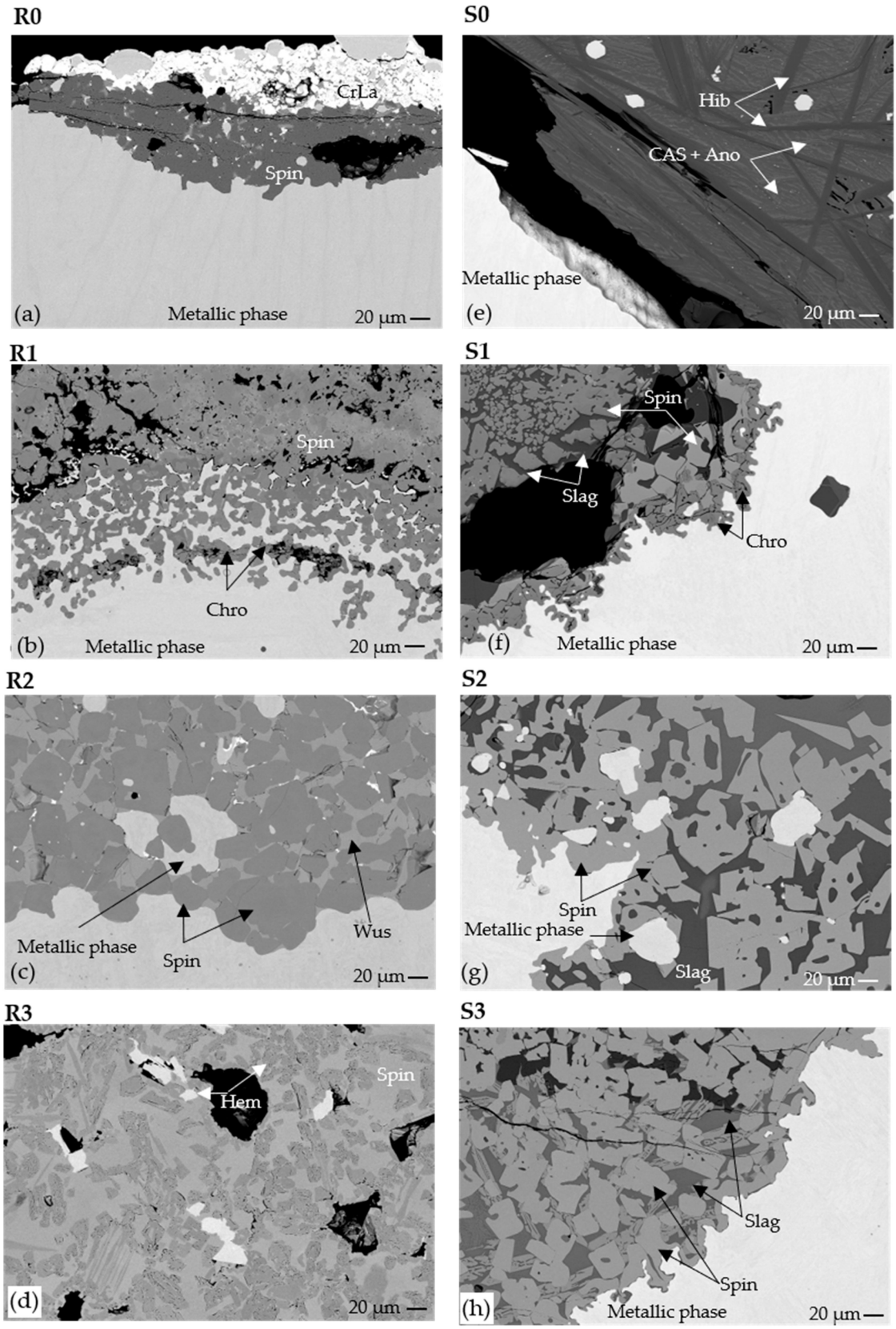

Figure 11. BSE images of microstructures of the oxide phases in remelted samples and smelted samples under (**a**,**e**) $P(O_2)$ = 0 bar, (**b**,**f**) 0.08 bar, (**c**,**g**) 0.17 bar, and (**d**,**h**) 0.33 bar, respectively. Mechanically entrained metallic phases were observed on oxide regions in R2 and S2. Short notations of the phase names are defined in Table 7.

In the remelted samples, spinel was found to be the predominant oxide phase. Spinel and lanthanum chromium oxides were present at inert conditions (R0, Figure 11a) due to inherent oxides as coatings, which likely dissolved and transformed into equilibrium oxides. In spinel structures, Cr consistently occupied the octahedral sites, while the tetrahedral sites contained substitutional Fe, Mn, and Ni atoms. Breakaway oxidation was observed in R1 (Figure 11b), where fragmented chromia phases were located directly at the alloy–oxide interface, while the spinel phase was approximately 40 µm away from the interface. Conversely, the spinel in R2 was in direct contact with the alloy and embedded within a wüstite matrix (Figure 11c). In R3, where complete oxidation occurred (Figure 11d), the spinel constituted the matrix with precipitated hematite grains.

In the smelted sample under inert conditions (Figure 11e), the observed oxide phases were likely transformation products of the CaO-SiO_2-Al_2O_3 slag system. Under oxidizing conditions, on the other hand (Figure 11f–h), spinel consistently appeared as the main oxide phase embedded in the slag matrix. The slag showed a relatively high amount of aluminum, indicating significant crucible dissolution. The stoichiometric formula of the spinel was similar to that observed in the remelted samples, with the addition of minor aluminum atoms occupying the octahedral sites. Chromium was found to be concentrated in the spinel phase, while the slag contained a very low amount of Cr (less than 2 wt.%) in all studied oxidizing conditions. As the amount of oxidized Fe increased as a function of $P(O_2)$, the amount of dissolved FeO in the slag also increased.

Overall, these observations strongly showed a high concentration of trivalent Cr oxidized in oxide spinel under the studied atmospheric conditions. Furthermore, the spinel phase exhibited high stability, embedded in either a wüstite or slag matrix or as the matrix itself.

Microstructural characteristics of alloy phases in remelted and smelted samples were also analyzed. BSE images of the microstructure of S0 (Figure 12a) demonstrated a two-phase microstructure consisting of a matrix and darker phases along the boundaries. Phase maps derived from EDS mapping of a region shown in Figure 12c are depicted in Figure 12d,e and highlight the distribution of delta-ferrite within the matrix. EBSD analysis revealed that this matrix was primarily composed of martensite with a minor amount of retained austenite, while the darker intergranular phase was confirmed to be delta-ferrite. These characteristics were also observed for sample R0. By contrast, the samples exposed to oxidizing conditions exhibited a predominantly single-phase matrix with a lath-martensitic microstructure, such as what is demonstrated in the BSE image of S1 in Figure 12b.

The ferrite matrix fractions for all samples are summarized in Figure 13. For the purpose of determining the overall alloy composition, the phase fractions between martensite and retained austenite comprising the matrix were not further distinguished since martensite possesses the same composition as the retained austenite. Elemental compositions were calculated from five EDS point analyses per phase, and the results are shown in Figure 14. The results suggested an overall decrease in Cr with increasing $P(O_2)$. However, it showed a steeper decline in remelted samples, from which complete Cr removal occurred at $P(O_2) = 0.17$ bar. Furthermore, there was a gradual increase in concentration of Fe, likely with Cr depletion until $P(O_2) = 0.17$ bar was reached, after which it showed a slightly decreasing trend in the case of smelted samples. Finally, Ni concentration had a gradually increasing trend, while cobalt concentration remained relatively constant for both remelted and smelted samples. Manganese concentration is not shown as it is too close to the detection limit of EDS analysis (<0.5 wt.%) to observe any clear trend. This experimental work demonstrated the drastic decrease in Cr content in the alloy, indicating its high susceptibility to oxidation towards the spinel phase under studied $P(O_2)$ conditions. Furthermore, the apparent ease of oxidation of elements was in the order of Cr > Fe > Co > Ni. To confirm this tendency, thermodynamic calculations were performed using FactSage 8.1 software.

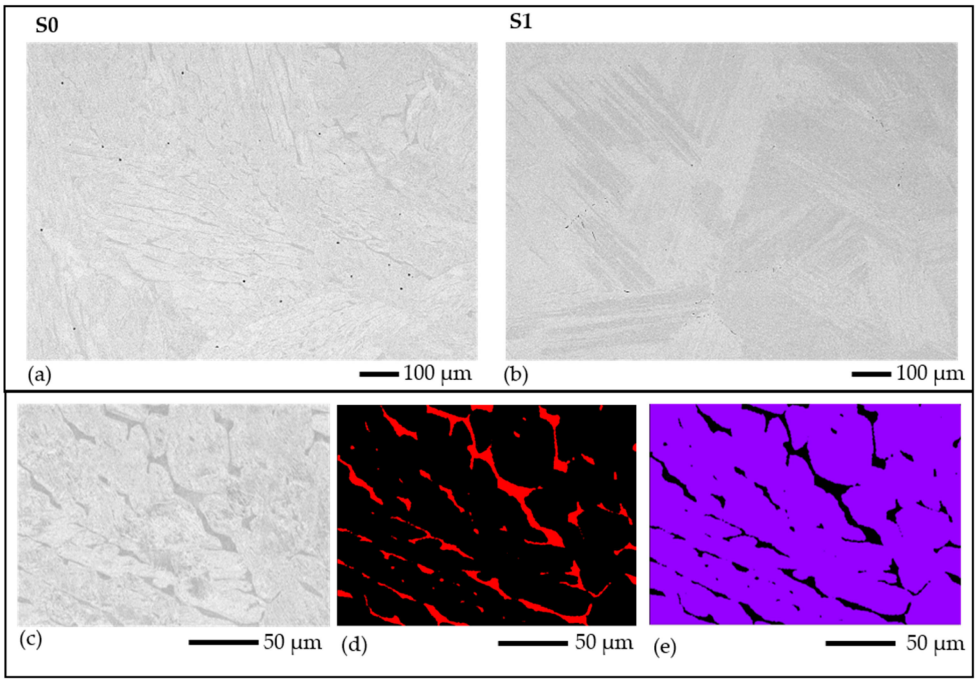

Figure 12. Microstructural BSE images of the alloy of smelted samples with sample codes (**a**) S0 and (**b**) S1; (**c**) BSE image, (**d**) delta-ferrite, and (**e**) matrix phase maps derived from EDS mapping of the alloy region in S0.

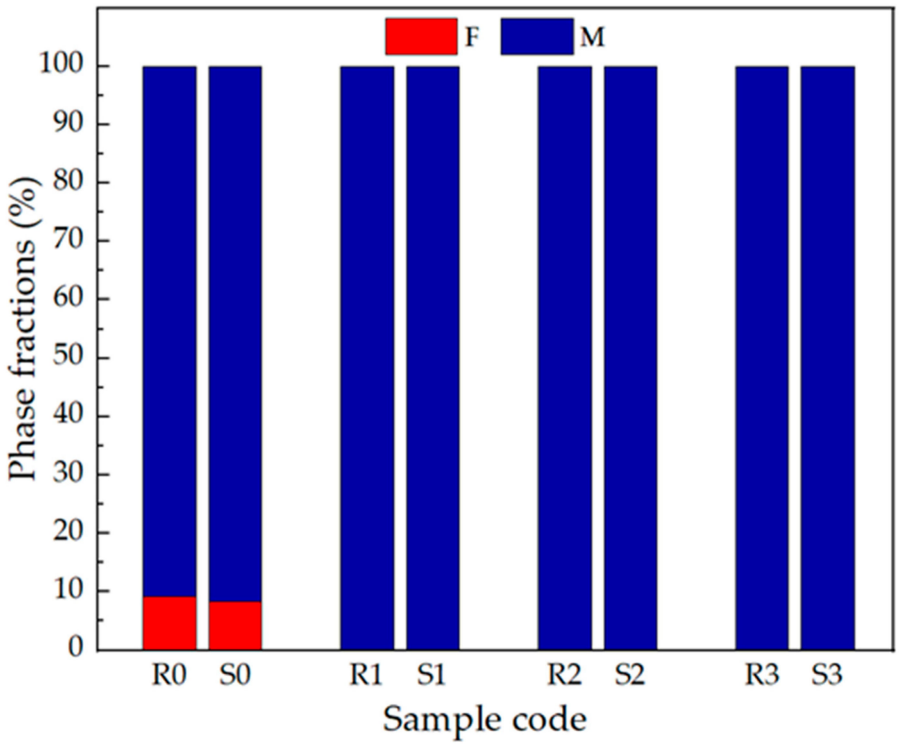

Figure 13. Phase fractions for all remelted and smelted samples, where F stands for ferrite, and M stands for the matrix (largely comprised of martensite with a minor amount of retained austenite).

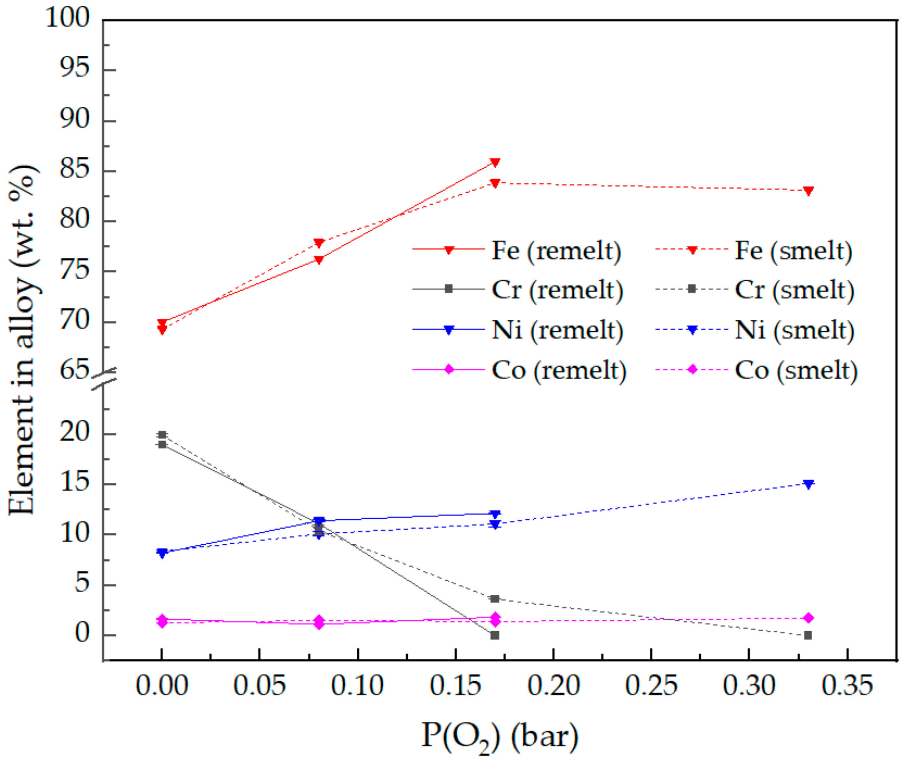

Figure 14. Elemental composition of remelted and smelted alloys at increasing $P(O_2)$.

3.4. Theoretical Element Distribution between Metallic and Oxide Phases

FactSage 8.1 was utilized to determine the element distribution in the equilibrium phases formed upon smelting of the blended composition described in Table 6 at 1600 °C under increasing oxygen partial pressures. The relative abundance of the most stable phases was calculated based on the Gibbs free energy minimization approach using available thermodynamic databases.

The distribution ratio, $L^{oxide/metal}$ of an element M during the smelting process, was defined as the ratio of the equilibrium concentration of M between the oxide phases (M_{oxide}) and solvent metal phase (M_{metal}). This ratio is represented by the following equation [27]:

$$L^{oxide/metal} = \frac{M_{oxide}(\text{wt.\%})}{M_{metal}(\text{wt.\%})}$$

Several authors defined the ratio as the partitioning of the element between the metal and slag [27–29]. However, the term "oxide" was used in this equation to include all the predicted oxide phases at equilibrium. A positive value indicates preferential partitioning of M to the oxide phases and hence favorable removal from the solvent metal phase. Figure 15 shows the logarithmic distribution ratios of input elements greater than 1 wt.%. Computation predicted that complete oxidization of liquid alloy occurs at $P(O_2) = 10^{-6}$ bar, where the graph ends. Notably, the ease of element oxidation is initially in the order Mn > Cr > Fe > Co > Ni from $P(O_2) = 10^{-15}$ to $P(O_2) = 10^{-10}$ bar. However, this changes to Cr > Mn > Fe > Co > Ni at higher oxygen partial pressures, which could be attributed to the formation of the cubic spinel from $P(O_2) = 10^{-10}$ bar that favorably oxidizes and consumes Cr. This order of oxidation confirms the experimental results in Figure 14.

The calculated equilibrium phase fractions and the element distribution under different oxygen partial pressures are shown in Figure 16. Only the main phases with relative abundance exceeding 2% are included in the analysis. Phase formulas are provided in Table 8. Caution was applied in comparing theoretical results with experimental data, as experimental conditions were also influenced by external factors such as mass transfer and reaction kinetics. As an example, the complete oxidation predicted at $P(O_2) = 10^{-6}$ bar

in equilibrium conditions contradicted the experimental data, wherein the alloy was still present at $P(O_2)$ = 0.33 bar. It is also crucial to note that the $P(O_2)$ values in equilibrium calculations do not directly correspond to those in Table 2. Instead, they are correlated to the oxygen potential experienced by the metallic and oxide phases in direct contact at thermodynamic equilibrium conditions. According to equilibrium calculations, transient phases such as corundum, silicate, wüstite, and tetragonal spinel occur at relatively low oxygen partial pressures ranging from $P(O_2) = 10^{-11}$ to 10^{-8} bar (Figure 16a). In contrast, cubic spinel and slag exhibit stability at high oxidizing conditions, with an increasing amount of cubic spinel as $P(O_2)$ rises. X-ray diffraction analysis (Figure 17) confirmed that this spinel in smelted samples exhibited a cubic structure with Fd-3m symmetry. Chromium shows consistent partitioning into the cubic spinel over the slag (Figure 16b), which was also observed experimentally. Iron partially partitions to wüstite at $P(O_2) = 10^{-8}$ bar before transitioning to the slag and cubic spinel phases. Manganese initially shows a preferential oxidation within the tetragonal spinel but tends to go to the slag at higher oxygen partial pressures. Finally, Ni and Co exhibit delayed complete oxidation, after which they partition between slag and cubic spinel phases.

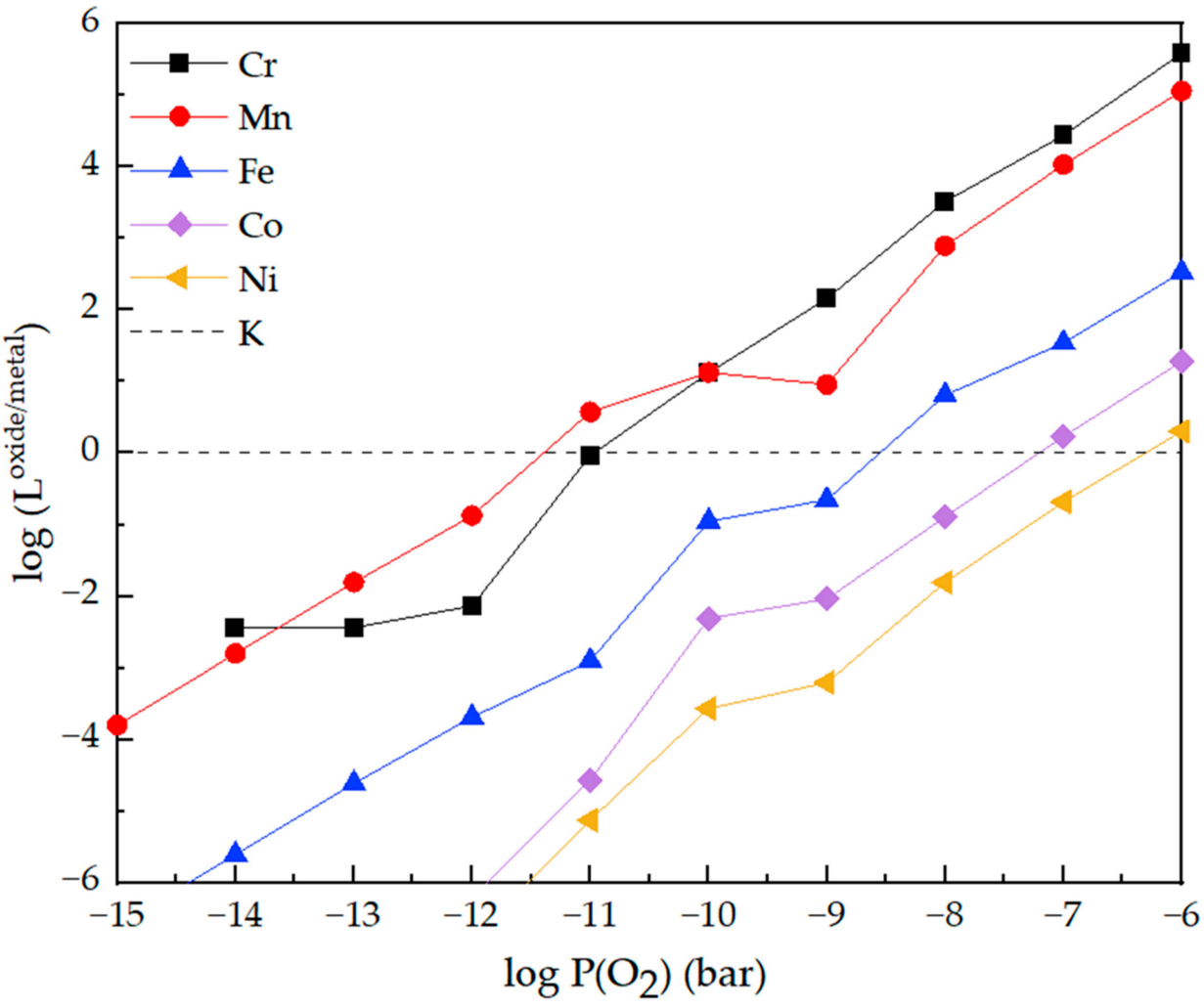

Figure 15. Logarithmic $L^{oxide/metal}$ values of main elements as a function of $P(O_2)$.

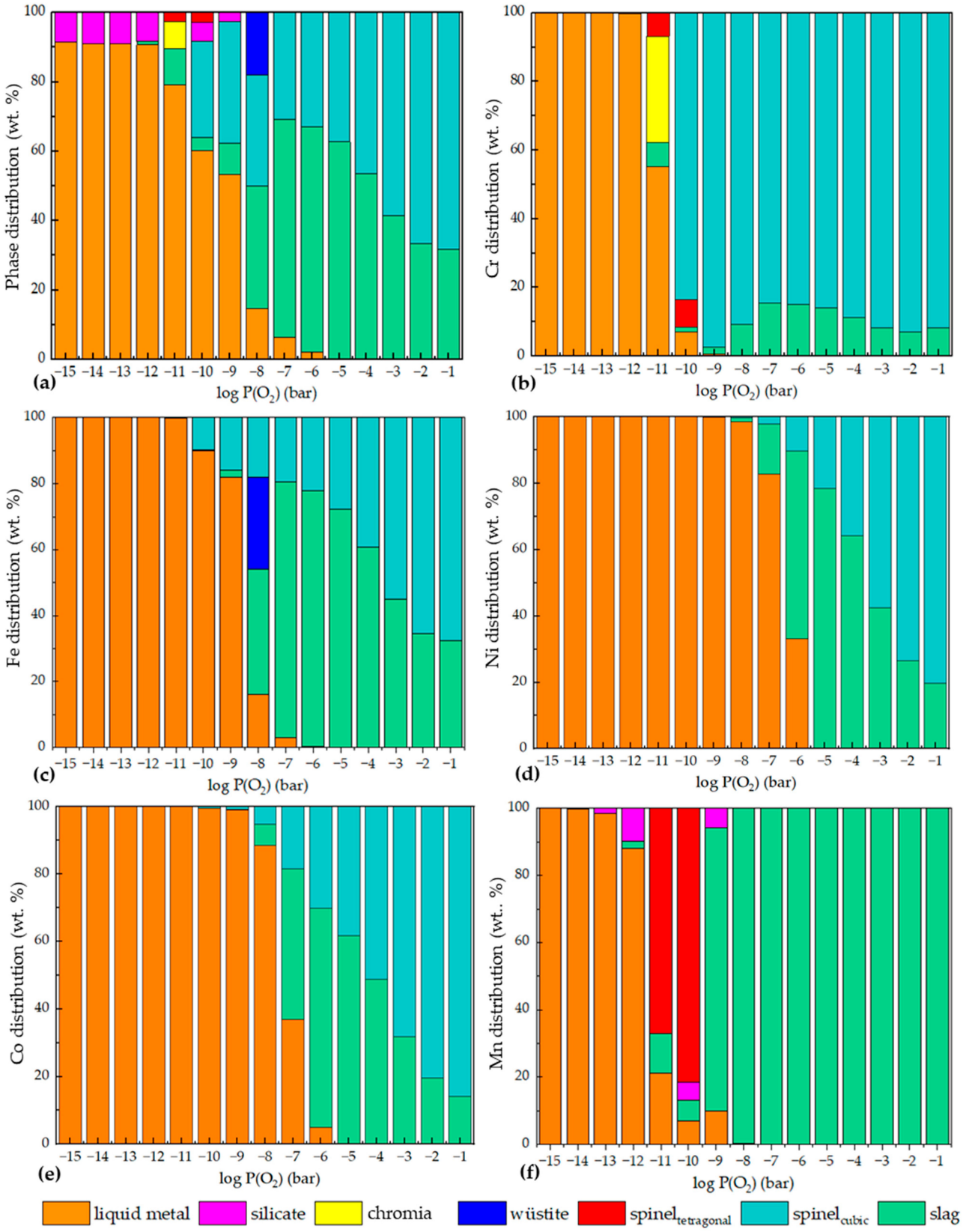

Figure 16. Normalized weight percent distribution of (**a**) calculated equilibrium phases at 1600 °C and the elements (**b**) Cr, (**c**) Fe, (**d**) Ni, (**e**) Co, and (**f**) Mn to such phases. Minor phases less than 2 wt.% are excluded.

Table 8. List of resulting equilibrium phases. Sublattice constituents with site fractions below 10^{-3} are excluded in the reference formula.

Phase	Reference Formula
Liquid metal	(Fe, Cr, Ni, Mn, Co)
Silicate	$(Ca^{+2}, Mn^{+2})_2(Si^{+4})(O^{-2})_4$
Chromia	$(Cr^{+3})_2(O^{-2})_3$
Wüstite	$(Fe^{+2})(O^{-2})$
$Spinel_{tetragonal}$	$(Cr^{+3}, Mn^{+2})_2(Cr^{+3})(O^{-2})_4$
$Spinel_{cubic}$	$(Cr^{+3}, Fe^{+2}, Fe^{+3}, Co^{+2}, Ni^{+2})_2(Fe^{+2}, Fe^{+3}, Cr^{+3}, Co^{+2}, Ni^{+2})(O^{-2})_4$
Liquid slag	$(Fe^{+2}, Fe^{+3}, Cr^{+2}, Cr^{+3}, Ni^{+2}, Co^{+2}, Mn^{+2}, Mn^{+3}, Si^{+4}, Ca^{+2})_x(O^{-2})_y$

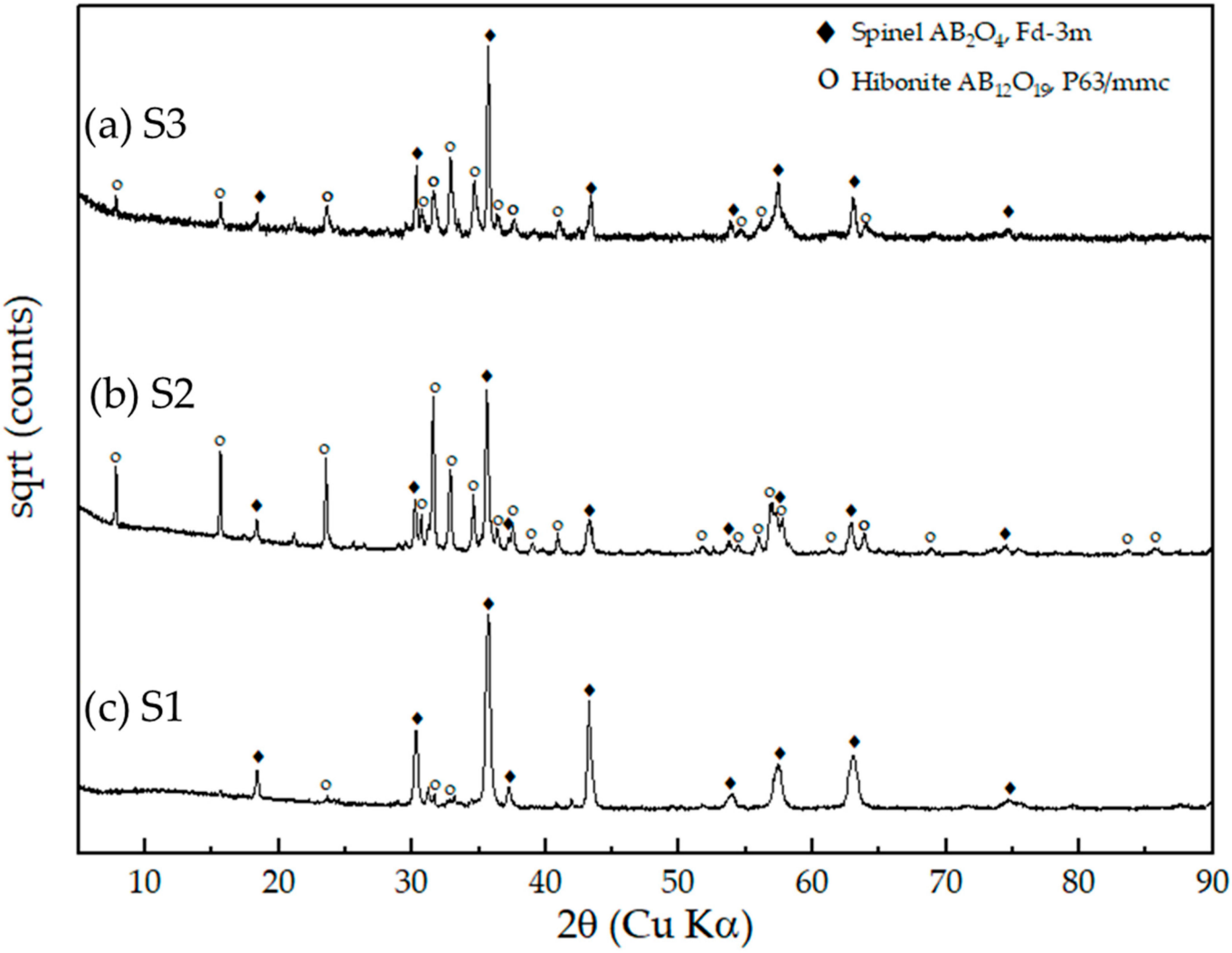

Figure 17. XRD patterns reveal the presence of spinel phases with cubic symmetry, denoted by filled diamonds, within the oxide regions of smelted samples with sample codes (**a**) S3, (**b**) S2, and (**c**) S1, respectively. The identified hibonite phases, represented by empty circles, are likely transformation products resulting from the crystallization of liquid slag.

Thermodynamic calculations and experimental findings (see Table 7 and Figures 11 and 16) consistently demonstrate the preferential partitioning of Cr to the spinel over the slag at high $P(O_2)$ values. Chromium is a critical component of stainless steels; thereby, strategies for its optimum recovery must be considered in process modeling. Furthermore, potential steel products, such as those specified in Table 5, do not have cobalt as an intentional alloying element. While nickel-containing stainless steels may unavoidably contain Co as a

trace element up to 0.3 wt.% [30], this value is below the measured Co concentration in the samples and must be reduced if this recycling pathway is taken. Nevertheless, Co remains a critical element in the production of technology materials, particularly in lithium-ion batteries [31,32]. Therefore, it is crucial to look into Co recovery rather than allowing it to be diluted within the alloy. Cobalt is exclusively present on the MCF oxide coating; hence, pretreatment techniques prior to steelmaking, such as blasting and pickling of end-of-life interconnectors, should be explored.

4. Conclusions

Experimental work was conducted to assess the composition of an end-of-life JÜLICH SOC stack interconnect assembly. Based on extensive characterization studies performed on the sample, the following conclusions were made:

- There was only a minor difference between the stoichiometric formulas of the standard coatings (LCC10 and MCF) and the coatings on the end-of-life interconnector.
- In addition to the coatings, thermally grown oxides Cr_2O_3 and Cr_2MnO_4 were observed on the coating–alloy and alloy–fuel gas boundaries.
- The interconnector was predominantly composed of iron and chromium with less than 4 wt.% of other alloying elements, mainly cobalt and manganese.
- Melting temperatures of the zonal specimens fell within the expected range for Crofer 22 APU alloy substrate, demonstrating negligible influence of the oxide coatings to the alloy's transition temperatures. The melting point of the nickel mesh was close to that of the pure nickel obtained from calibration, indicating the mesh's high purity.
- Stainless steels in the 4xx, 2xx, and 3xx AISI series can be potentially produced based on the calculated blended compositions with and without the addition of nickel meshes.

Furthermore, the feasibility of recovering metallic resources from the end-of-life JÜLICH SOC stack interconnect assembly was evaluated. This was performed through small-scale remelting and smelting experiments on samples representative of the interconnect assembly and thermodynamic equilibrium calculations. Based on the results, the following conclusions were made:

- Smelted samples had an overall lower degree of oxidation than remelted samples within the studied $P(O_2)$ conditions (0–0.33 bar), which confirms the practical and beneficial effects of the oxide fluxes in suppressing oxidation.
- There was an overall decrease in chromium as a function of $P(O_2)$ relative to other elements in both remelted and smelted alloys. Iron concentration increased from $P(O_2) = 0$ to 0.17 bar, beyond which it showed a slightly decreasing trend. Nickel concentration was observed to have a consistently increasing trend, while the cobalt concentration remained constant.
- Chromium preferentially oxidized and partitioned to the cubic spinel over the slag at high $P(O_2)$ values. Chromium is a critical component of stainless steels; thereby, strategies for its optimum recovery must be explored.
- Thermodynamic calculations using FactSage 8.1 predicted an ease of element oxidation, quantified by distribution ratios, in the order of Mn > Cr > Fe > Co > Ni from $P(O_2) = 10^{-15}$ to $P(O_2) = 10^{-10}$ bar, but this changes to Cr > Mn > Fe > Co > Ni at higher oxygen partial pressures. This switch could be attributed to the formation of the cubic spinel from $P(O_2) = 10^{-10}$ bar that favorably consumes chromium.
- Potential steel products do not contain cobalt as an alloying element. Cobalt is nevertheless a key component in energy applications and therefore must be recovered rather than permitted to be lost through alloy dilution.

Future work will involve comparing such characterization results with interconnectors from other end-of-life SOC stack designs and manufacturers. Additionally, a recycling route based on scrap-based steelmaking operations with pretreatment steps for contamination control will be explored to transform interconnector assemblies into steel products that meet existing market demands.

Author Contributions: Conceptualization, J.L. and D.S.; methodology, J.L. and D.S.; investigation, J.L., D.S. and D.G.; resources, D.S. and M.M.; data curation, J.L. and D.S.; writing—original draft preparation, J.L.; writing—review and editing, D.S., D.G., M.M. and R.S.; visualization, J.L. and D.S.; supervision, D.S. and M.M.; project administration, M.M. and R.S.; funding acquisition, M.M. and R.S. All authors have read and agreed to the published version of the manuscript.

Funding: This research was funded by the German Federal Ministry of Education and Research (BMBF) under the grant number FKZ 03HY111J for the "ReNaRe" project as part of the technology platform H_2Giga.

Data Availability Statement: The original contributions presented in the study are included in the article. Further inquiries can be directed to the corresponding authors.

Acknowledgments: The authors acknowledge the support provided by the following staff of Forschungszentrum Jülich GmbH: F. Schulze-Küppers (interconnect assembly sample provision), V. Gutzeit (metallographic sample preparation), E. Yazhenskikh (thermodynamic calculations), E. Wessel (microstructural analysis), M. Ziegner (X-ray diffraction analysis), and N. Menzler (discussions and support of the framework of the "ReNaRe" project).

Conflicts of Interest: Author Dmitry Sergeev was employed by the company NETZSCH-Gerätebau GmbH. The remaining authors declare that the research was conducted in the absence of any commercial or financial relationships that could be construed as a potential conflict of interest.

References

1. IEA. *Global Hydrogen Review 2021*; International Energy Agency: Paris, France, 2021; pp. 18–20.
2. Wappler, M.; Unguder, D.; Lu, X.; Ohlmeyer, H.; Teschke, H.; Lueke, W. Building the Green Hydrogen Market—Current State and Outlook on Green Hydrogen Demand and Electrolyzer Manufacturing. *Int. J. Hydrogen Energy* **2022**, *47*, 33551–33570. [CrossRef]
3. IRENA. *Global Hydrogen Trade to Meet the 1.5 °C Climate Goal: Part I—Trade Outlook for 2050 and Way Forward*; International Renewable Energy Agency: Abu Dhabi, United Arab Emirates, 2022; pp. 38–67.
4. BMWK. *The National Hydrogen Strategy*; Federal Ministry for Economic Affairs and Energy: Berlin, Germany, 2020; pp. 2–6.
5. BMBF H2Giga: Serienfertigung. Available online: https://www.wasserstoff-leitprojekte.de/leitprojekte/h2giga (accessed on 31 October 2022).
6. DECHEMA ReNaRe Recycling—Nachhaltige Ressourcennutzung. Available online: https://dechema.de/Forschung/Projekte/ReNaRe.html (accessed on 31 May 2023).
7. Andersson, M.; Sunden, B. *Technology Review—Solid Oxide Fuel Cell*; Energiforsk: Stockholm, Sweden, 2017; pp. 11–28.
8. Zhu, W.Z.; Deevi, S.C. Development of Interconnect Materials for Solid Oxide Fuel Cells. *Mater. Sci. Eng. A* **2003**, *348*, 227–243. [CrossRef]
9. Blum, L.; Meulenberg, W.; Nabielek, H.; Steinberger-Wilckens, R. Worldwide SOFC Technology Overview and Benchmark. *Int. J. Appl. Ceram. Technol.* **2005**, *2*, 482–492. [CrossRef]
10. ThyssenKrupp VDM. *Crofer®22 H*; ThyssenKrupp VDM GmbH: Werdohl, Germany, 2010.
11. Bianco, M.; Ouweltjes, J.P.; Herle, J.V. Degradation Analysis of Commercial Interconnect Materials for Solid Oxide Fuel Cells in Stacks Operated up to 18000 Hours. *Int. J. Hydrogen Energy* **2019**, *44*, 31406–31422. [CrossRef]
12. Talic, B.; Molin, S.; Hendriksen, P.V.; Lein, H.L. Effect of Pre-Oxidation on the Oxidation Resistance of Crofer 22 APU. *Corros. Sci.* **2018**, *138*, 189–199.
13. Ghiara, G.; Piccardo, P.; Bongiorno, V.; Repetto, L.; Geipel, C.; Spotorno, R. Characterization of Metallic Interconnects Extracted from Solid Oxide Fuel Cell Stacks Operated up to 20,000 h in Real Life Conditions: The Fuel Side. *Int. J. Hydrogen Energy* **2021**, *46*, 23815–23827. [CrossRef]
14. Linder, M.; Hocker, T.; Holzer, L.; Friedrich, K.A.; Iwanschitz, B.; Mai, A.; Schuler, J.A. Cr2O3 Scale Growth Rates on Metallic Interconnectors Derived from 40,000 h Solid Oxide Fuel Cell Stack Operation. *J. Power Sources* **2013**, *243*, 508–518. [CrossRef]
15. Malzbender, J.; Batfalsky, P.; Vaßen, R.; Shemet, V.; Tietz, F. Component Interactions after Long-Term Operation of an SOFC Stack with LSM Cathode. *J. Power Sources* **2012**, *201*, 196–203. [CrossRef]
16. Groß-Barsnick, S.M.; Fang, Q.; Batfalsky, P.; Niewolak, L.; Blum, L.; Quadakkers, W.J. Post-Test Characterization of Metallic Materials and Adjacent Components in an SOFC Stack After 34,000 h Operation at 700 °C. *Fuel Cells* **2019**, *19*, 84–95. [CrossRef]
17. Niewolak, L.; Blum, L.; Peters, R.; Grüner, D.; Quadakkers, W.J. Behavior of Metallic Components During 4000 h Operation of an SOFC Stack with Carbon Containing Fuel Gas. *Fuel Cells* **2016**, *16*, 600–610. [CrossRef]
18. Sarner, S.; Schreiber, A.; Menzler, N.H.; Guillon, O. Recycling Strategies for Solid Oxide Cells. *Adv. Energy Mater.* **2022**, *12*, 2201805. [CrossRef]
19. Yenesew, G.T.; Quarez, E.; SALLE, A.L.G.L.; Nicollet, C.; Joubert, O. Recycling and Characterization of End-of-Life Solid Oxide Fuel/Electrolyzer Ceramic Material Cell Components. *Resour. Conserv. Recycl.* **2023**, *190*, 106809. [CrossRef]
20. Sarner, S.; Menzler, N.H.; Hilgers, A.; Guillon, O. Recycling and Reuse Strategies for Ceramic Components of Solid Oxide Cells. *ECS Trans.* **2023**, *111*, 1369–1378. [CrossRef]

21. Xiao, Y.; Holappa, L. Distribution of Chromium between Slag and Metal. In *Thermodynamic Properties of Chromium Bearing Slags and Minerals*; Helsinki University of Technology: Espoo, Finland, 1996; pp. 39–42, ISBN 951-22-3170-0.
22. Engh, T.A.; Sigworth, G.K.; Kvithyld, A. Converter Processes for Steelmaking–Refining of Stainless Crude Steel. In *Principles of Metal Refining and Recycling*; Oxford University Press: Oxford, UK, 2021; pp. 567–573, ISBN 978-0-19-881192-3.
23. Xiao, Y.; Wei, K.; Wang, L.; Liu, S.; He, X.; Chou, K. Influence of Slag Chemistry on the Dissolution of $FeCr_2O_4$ in CaO–SiO_2–Al_2O_3–MgO Slag with Graphite Crucible. *ISIJ Int.* **2023**, *63*, 613–621. [CrossRef]
24. VDM Metals VDM®. *Crofer 22 APU Crofer 22 APU*; VDM Metals: Werdohl, Germany, 2022.
25. Haynes, W.M.; Lide, D.R.; Bruno, T.J. Properties of the Elements and Inorganic Compounds. In *CRC Handbook of Chemistry and Physics*; Taylor & Francis Group: Boca Raton, FL, USA, 2014; pp. 1–43.
26. Euro Inox. *Stainless Steel: Tables of Technical Properties*, 2nd ed.; Materials and Applications; Euro Inox: Luxembourg, 2007; Volume 5, ISBN 978-2-87997-242-8.
27. Pagador, R.U.; Hino, M.; Itagaki, K. Distribution of Minor Elements between MgO Saturated FeOx–MgO–SiO_2 or FeOx–CaO–MgO–SiO_2 Slag and Nickel Alloy. *Mater. Trans. JIM* **1999**, *40*, 225–232.
28. Li, G.; Tsukihashi, F. Distribution Equilibria of Fe, Co and Ni between MgO-Saturated FeO_x–MgO–SiO_2 Slag and Ni Alloy. *ISIJ Int.* **2001**, *41*, 1303–1308. [CrossRef]
29. Avarmaa, K.; Taskinen, P.; Klemettinen, L.; O'Brien, H.; Lindberg, D. Ni-Fe-Co Alloy -Magnesia-Iron-Silicate Slag Equilibria and the Behavior of Minor Elements Cu and P in Nickel Slag Cleaning. *J. Mater. Res. Technol.* **2021**, *15*, 719–730. [CrossRef]
30. Wang, X.; Hedberg, J.; Nie, H.-Y.; Biesinger, M.C.; Odnevall, I.; Hedberg, Y.S. Location of Cobalt Impurities in the Surface Oxide of Stainless Steel 316L and Metal Release in Synthetic Biological Fluids. *Mater. Des.* **2022**, *215*, 110524. [CrossRef]
31. Barker, J. Lithium-Ion Rechargeable Batteries: Novel Materials. In *Encyclopedia of Materials: Science and Technology*; Buschow, K.H.J., Cahn, R.W., Flemings, M.C., Ilschner, B., Kramer, E.J., Mahajan, S., Veyssière, P., Eds.; Elsevier: Oxford, UK, 2010; pp. 1–6, ISBN 978-0-08-043152-9.
32. Lebrouhi, B.E.; Baghi, S.; Lamrani, B.; Schall, E.; Kousksou, T. Critical Materials for Electrical Energy Storage: Li-Ion Batteries. *J. Energy Storage* **2022**, *55*, 105471. [CrossRef]